1 **Synoptic fluctuation of the Taiwan Warm Current in winter on the East China Sea shelf**

2 Jiliang Xuan[1], Daji Huang[1, 2], Thomas Pohlmann[3], Jian Su[3], Bernhard Mayer[3], Ruibin Ding[2,1], Feng Zhou[1, 2]

3

4 [1]State Key Laboratory of Satellite Ocean Environment Dynamics, Second Institute of Oceanography,

5 State Oceanic Administration, Hangzhou, China

6 [2]Ocean College, Zhejiang University, Zhoushan, China

7 [3]Institute of Oceanography, University of Hamburg, Hamburg, Germany

8 *Correspondence to:* Daji Huang (djhuang@sio.org.cn)

9 **Highlights**

10 ● Synoptic fluctuations of the wintertime Taiwan Warm Current appear mainly in two areas: north of

11 Taiwan and the inshore area

12 ● Synoptic fluctuation is mainly driven by the Taiwan Strait Current north of Taiwan and by wind in

13 the inshore area

14 ● Large Taiwan Strait Current intrusion generates a cross-shore transport from the coastal area to the

15 offshore area

16 ● Winter monsoon affects the alongshore transport of Taiwan Warm Current water between the 30

17 and 100 m isobaths

18 ● Winter monsoon affects the cross-shore transport of Taiwan Warm Current water at the latitudes

19 26.5 ˚N and 28 ˚N

20

21 **Abstract.** The seasonal mean and synoptic fluctuation of the wintertime Taiwan Warm Current (TWC)

22 were investigated using a well validated finite volume community ocean model. The spatial distribution

23 and dynamics of the synoptic fluctuation were highlighted. The seasonal mean of the wintertime TWC

24 has two branches: an inshore branch between the 30 and 100 m isobaths and an offshore branch between

25 the 100 and 200 m isobaths. The Coriolis term is much larger than the inertia term and is almost balanced

26 by the pressure gradient term in both branches, indicating geostrophic balance of the mean current. Two

27 areas with significant fluctuations of the TWC were identified during wintertime. One of the areas is

28 located to the north of Taiwan with velocities varying in the cross-shore direction. These significant

29 cross-shore fluctuations are driven by barotropic pressure gradients associated with the intrusion of the

30 Taiwan Strait Current (TSC). When a strong TSC intrudes to north of Taiwan, the isobaric slope tilts

31 downward from south to north, leading to a cross-shore current from the coastal area to the offshore area.

32 When the TSC intrusion is weak, the cross-shore current to the north of Taiwan is directed from offshore

33 to inshore. The other area of significant fluctuation is located in the inshore area between the 30 and 100

34 m isobaths. The fluctuations are generally strong both in the alongshore and cross-shore directions, in

35 particular at the latitudes 26.5 °N and 28 °N. Wind affects the synoptic fluctuation through episodic events.

36 When the northeasterly monsoon prevails, the southwestward Zhe-Min Coastal Current dominates the

37 inshore area associated with a deepening of the mixed layer. When the winter monsoon is weakened or

38 the southwesterly wind prevails, the northeastward TWC dominates in the inshore area.

39

42

1 Introduction

On the East China Sea (ECS) shelf, the mean path of the Taiwan Warm Current (TWC) has two branches: the inshore branch along the 50 m isobath and the offshore branch along the 100 m isobath (Su and Pan, 1987). The summer TWC has been well studied because the current is stationary and strong, with an average speed of 0.3 m/s (Guan, 1978; Fang et al., 1991; Isobe, 2008; Yang et al., 2011, 2012). The spatial structure and temporal variation of the wintertime (December to March) TWC are less known due to its weak mean surface velocity, according to a climatological structure of the surface current in the ECS mapped by Qiu and Imasato (1990).

The wintertime TWC on the ECS shelf shows synoptic fluctuations (Cui et al., 2004; Zhu et al., 2004; Zeng et al., 2012; Huang et al., 2016). These synoptic fluctuations show some features common with those over other continental shelves, i.e., they have periods between 3 and 15 days and are associated with coastal sea level changes, which can be explained by local winds or by coastal trapped waves (Huyer, 1990; Brink, 1991; Huthnance et al., 1986). Huang et al. (2016) have shown that the wind was a main physical factor which caused the temporal variation of the wintertime currents at the synoptic scale in the coastal area of the ECS. However, the dominant physical factors of the TWC fluctuations still lack study; the fluctuations on the whole shelf of the ECS may be complicated due to the complex bottom topography, alternating wind forcing and conjunction of several current systems such as the Kuroshio Current, the Taiwan Strait Current (TSC) and the Zhe-Min Coastal Current (ZMCC). These synoptic fluctuations are also known to influence the regional material transport, especially when the amplitude of the fluctuations is comparable to, or even larger than, the mean current. On the ECS shelf, some recent

3

65   observations have shown that the TWC has an episodic wintertime feature (Zhu et al., 2004) and the

66   variations of the TWC in winter have an amplitude as large as 0.2 m/s (Zeng et al., 2012). Moreover, it

67   has been observed that the variations of the TWC in winter cause a cross-shore current which is closely

68   linked to the alongshore component (Huang et al., 2016). Therefore, we focus on studying the spatial

69   patterns of synoptic fluctuations to better understand the role of the wintertime TWC on the cross-shore

70   water exchange.

71

72   A comparison between the wintertime climatological density (Fig. 1a) and synoptic density distributions

73   observed during two surveys (Figs. 1b and 1c) suggests that two distinct areas with significant synoptic

74   fluctuations exist. The climatological density is taken from the Generalized Digital Environment Model

75   (GDEM, Carnes, 2009) data, and the two surveys were carried out in February 2007 by two research

76   vessels. Because the isopycnal lines are closely related to geostrophic currents, we can infer the strength

77   of the TWC from the horizontal gradient of the isopycnals between 24-σ_t and 25-σ_t contours (Fig. 1a).

78   This accounts for the fact that in winter the water mass of TWC is located in this density range [according

79   to the hydrography analysis of Su et al. (1994)]. The two-branch structure of the TWC can be inferred

80   from the wintertime climatological density. In this paper, we defined that the near-coast area is the area

81   between the coast and 30 m isobath where the ZMCC occurs; the inshore area is the area between the 30

82   and 100 m isobaths where the TWC inshore branch dominates; and the offshore area is the region between

83   the 100 and 200 m isobaths where the TWC offshore branch prevails. According to the hydrographic

84   data analysis and numerical interpretation by Su and Pan (1987), the TWC inshore and offshore branches

85   mainly occur close to those specific isobaths. However, these two branches were missing during the two

86   synoptic surveys (Figs. 1b and 1c), indicating strong synoptic fluctuations of the TWC on the ECS shelf.

4

87   Furthermore, the density anomalies between the two surveys and the GDEM data (Figs. 1d and 1e)

88   indicate that the most significant fluctuations are located north of Taiwan and in the inshore area. Both

89   surveys show negative density anomalies north of Taiwan, indicating that the TWC was weak and that

90   more low-density coastal water was transported to the ECS shelf during the observational periods. The

91   density anomalies in the inshore area show different patterns for the two synoptic surveys, with a positive

92   anomaly in the first survey (Fig. 1d) and a negative anomaly in the second (Fig. 1e), indicating a strong

93   synoptic fluctuation in the inshore area.

94

95 | Figure 1 |
      | --- |
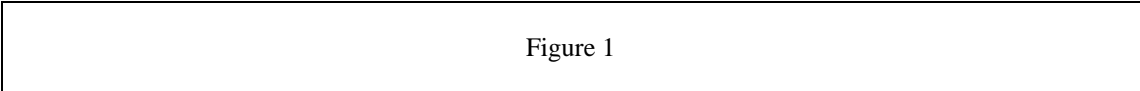
96

97   Candidate factors for driving these synoptic fluctuations are local wind, surface cooling, and the upstream

98   currents of the Kuroshio Current and the TSC. As discussed by Huyer (1990), wind is often considered

99   as the major driving mechanism of synoptic fluctuations of the wintertime TWC. The northeasterly

100   monsoon wind in winter blows against the northeastward TWC and produces a southwestward ZMCC

101   (Chuang and Liang, 1994; Oey et al., 2010). Zhu et al. (2004) suggested that the occurrence and duration

102   of the TWC are associated with the meandering of the Kuroshio Current north of Taiwan. The

103   northeastward TSC, as an upstream flow of the TWC, also influences the synoptic fluctuation of the

104   wintertime TWC. Hong et al. (2011) and Hu et al. (2010) summarized that the temporal and spatial

105   variation of TSC is modulated by strong wind forcing, complex topography and circulation in the

106   northern South China Sea as well as coastal water input and the Kuroshio intrusion. Guan and Fang (2006)

107   showed evidence that the TSC and the TWC merge in the area between the Taiwan Strait and the Zhe-

108   Min coastal region. Takahashi and Morimoto (2013) pointed out that the temporal variation of the TWC

109   is characterized by the propagation of vorticity anomalies originating from northeast of the Taiwan Strait,

110   which further demonstrated that the fluctuations of TWC was associated with its upstream currents such

111   as the TSC.

112

113   To explore the spatial distribution of synoptic fluctuations of the wintertime TWC on the ECS shelf,

114   current data with high resolution in both space and time are required. Previous studies on the wintertime

115   TWC were based on cruise surveys (Su and Pan, 1987; Chen et al., 1994; Chen and Wang, 1999),

116   anchored mooring observations (Zhu et al., 2004; Zeng et al., 2012; Huang et al., 2016) and numerical

117   simulations (Guo et al., 2003, 2006; Yang et al., 2011, 2012; Xuan et al., 2012, 2016). The observation

118   data are limited in terms of temporal and spatial coverage; hence, they cannot fully reveal the synoptic

119   fluctuations of the TWC and their regional differences. Numerical simulations provide a promising

120   approach for studying the overall structure and driving mechanisms of synoptic fluctuations of the TWC

121   in more detail.

122

123   In this study, the Finite Volume Coastal Ocean Model (FVCOM; Chen et al., 2003) is used to investigate

124   wintertime TWC synoptic fluctuations and their mechanisms. The rest of this paper is organized as

125   follows. In Sect. 2, we provide a description of methods and validation. The mean distribution, synoptic

126   fluctuations, and dynamic diagnostics of the wintertime TWC are given in Sect. 3. The impact of synoptic

127   fluctuation on water exchange is further discussed in Sect. 4, followed by conclusions in Sect. 5.

128

129 **2 Methods and validation**

130 **2.1 Model configuration**

131 To investigate the currents (TWC, Kuroshio Current, ZMCC, etc.) and their synoptic fluctuations on the

132 ECS shelf, a 3-D unstructured-grid (Fig. 2, left panel) FVCOM is developed for the entire Bohai, Yellow,

133 and East China Seas (part of the Japan/East Sea, and part of the Pacific Ocean). A regional refinement of

134 the resolution (approximately 3 km) is specified around the ECS shelf break at the 200 m isobaths, where

135 a strong excursion of the Kuroshio Current also occurs. The General Bathymetric Chart of the Oceans

136 (GEBCO) provides high-resolution (approximately 1 km) bathymetric data (Smith and Sandwell, 1997).

137 Twenty vertical layers with 76954 triangle cells were specified in the water column in a sigma-stretched

138 coordinate system.

139

140 The driving forces of the numerical simulation include tides, river discharge, surface heat fluxes, wind,

141 and open boundary conditions. Harmonic constants of 11 major tidal constituents (M_2, S_2, N_2, K_2, K_1, O_1,

142 P_1, Q_1, M_4, MS_4, and MN_4) were used; these are based on the Oregon State University global inverse

143 tidal model TPXO.7.0 (Egbert et al., 1994; Egbert and Erofeeva, 2002). The daily-mean river discharge

144 of the Changjiang and Huanghe were taken from publicly available observation data at the Datong

145 hydrometric station (http://yu-zhu.vicp.net/). Other rivers were not included because of their small

146 discharges, e.g., the Qiantang River, with the largest runoff from the Zhejiang coast, has a climatological

147 mean discharge in winter of about 230 m^3/s, which is nearly negligible compared to the Changjiang

148 winter discharge of about 11500 m^3/s. The daily-mean heat fluxes were from the objectively analyzed

149 air–sea fluxes (Yu and Weller, 2007), and the 3-hourly wind stress and 10 m wind speed data was from

150 the ERA-40 re-analysis (Uppala et al., 2005). The open boundary conditions, including daily temperature,

7

151   salinity, and fluxes at the Taiwan Strait, the western Pacific Ocean, and the Japan/East Sea, were obtained

152   from the Hybrid Coordinate Ocean Model (Bleck, 2002) and interpolated onto the FVCOM model grid

153   points. The temporal resolution of all the driving force fields is better than or equal to one day, which is

154   essential to resolve synoptic fluctuations.

155

156   The hindcast outputs of sea surface height, temperature, salinity, and velocities for the five years of

157   simulation from 2009 to 2013 are used, following three spin-up years (2006-2008) initiated with the

158   temperature and salinity taken from the Hybrid Coordinate Ocean Model and velocity set to zero. The

159   initial conditions are ramped-up over a period of 30 days and at the lateral boundaries a sponge layer was

160   used with the same method as Chen et al. (2008). The model time step was 15 seconds for the 2-D

161   barotropic mode and 90 seconds for the 3-D baroclinic mode. All of the output fields were processed

162   with a tidal filter (Godin, 1972) to remove tidal oscillations (considering that the major time scale of

163   synoptic fluctuations in this study area is 3–15 days).

164

165   Since the currents in 2009 could partly be validated by means of available observational data (see Sect.

166   2.2), the currents from January 1 to February 28, 2009 were selected for analysis of the wintertime TWC.

167

168   **2.2 Validation of the mean currents and synoptic fluctuations**

169   The mean currents, e.g., the Kuroshio Current, the TWC, and the ZMCC, were calculated by averaging

170   the outputs of January and February 2009. We validated the mean currents in terms of circulation

171   structure, boundary fluxes, and coastal currents.

172

173   The FVCOM has reproduced almost all of the known circulation structure in the ECS in winter. The

174   surface mean currents (Fig. 2) shows three major currents: the Kuroshio Current, the TWC, and the

175   ZMCC. The Kuroshio Current, with a speed of about 1 m/s, enters the ECS just northeast of Taiwan and

176   flows along the shelf break up to the northern area and ultimately leaves the ECS through the Tokara

177   Strait. Both the route and strength of the Kuroshio are comparable with those reported in the literature

178   (Guan, 1978; Qiu and Imasato, 1990). The TWC has two northeastward branches, one inshore (between

179   the 30 and 100 m isobaths) and another offshore (between the 100 and 200 m isobaths), which is

180   consistent with Su and Pan (1987). The southwestward directed ZMCC in the nearshore area from the

181   Changjiang Estuary to the Taiwan Strait agrees well with that reported in previous studies (Guan and

182   Mao, 1982; Zeng et al., 2012).

183

184   The simulated volume transports across the Taiwan Strait, the East Taiwan Channel, the Tsushima Strait,

185   the Tokara Strait, and the shelf break of the 200 m isobath were validated using results from the literature

186   (Table 1). The simulated transports were accurate enough to reproduce volume transport (1.22 Sv)

187   through the Taiwan Strait which is closer to the observation value (1.20 Sv) from Isobe (2008) than

188   former model results. The volume transports across the Taiwan Strait and the Tokara Strait, and the cross-

189   shore exchange, affected the path and magnitude of the TWC. The annual mean transport across the 200

190   m isobath toward the shelf is 1.66 Sv, which is balanced by the inflow from the Taiwan Strait (1.22 Sv)

191   and the outflow through the Tsushima Strait (2.85 Sv).

192

193   Figure 2

194

9

195 | Table 1

196

197 Figure 3 shows a comparison between simulation and observation results for the alongshore currents and

198 the cross-shore currents on the ECS shelf. The observational data were obtained from four mooring

199 surveys (Fig. 2, red stations) off the Zhe-Min coast (Zeng et al., 2012). The observed and simulated

200 currents were both averaged for the observational period, which was from January 1 to February 28,

201 2009. Using the same method as in Huang et al. (2016), we defined the positive alongshore current

202 direction as from southwest (218°) to northeast (38°), which is the mean tangential direction of the

203 isobaths on the southwestern shelf of the ECS. The positive cross-shore direction is from northwest (308°)

204 to southeast (128°), normal to the isbaths. The alongshore components (Figs. 3a and 3b) show that the

205 ZMCC flows southwestward parallel to the coast in winter, with a maximum speed of 0.15 m/s along the

206 30 m isobath. The TWC flows northeastward with a speed of 0.05 m/s, and the core is located in the

207 lower layer at about 50 m at Station 4. The cross-shore component (Figs. 3c and 3d) is much weaker than

208 the alongshore components, and it shows a complex spatial pattern. It flows offshore in the upper layer

209 and onshore in the lower layer at Station 1. Moreover, it mainly flows onshore at Station 2, and it flows

210 offshore in the entire water column at Stations 3 and 4. Altogether, the simulated pattern and magnitude

211 both of the alongshore and cross-shore components are in good agreement with the observations.

212 However, there are some differences between the observed and simulated results; for example, the

213 simulated ZMCC occupies a broader space than that in the observations. This may have been caused by

214 the relatively low number of observational stations.

215

216 | Figure 3

217

218   Synoptic fluctuations of the TWC inshore branch during January and February 2009 were also validated

219   against the mooring results (Fig. 4). Since the TWC shows a strong signature at Station 4, the time series

220   of the alongshore currents and cross-shore currents in the whole water column of Station 4 were used for

221   the validation. To eliminate the influence of local effects, the simulated currents were averaged in a $10 \times$

222    $10 \ km^2$ area around Station 4. Both the observed and simulated results show that the TWC fluctuates

223   with a period of 3–15 days. The simulated TWC (Fig. 4a, warm color) appeared stronger (> 0.1 m/s) on

224   Jan. 7, Jan. 12, Jan. 18, Jan. 21, Jan. 26, Jan. 29, Feb. 10, Feb. 14, Feb. 19, Feb. 22, and Feb. 25, which

225   agrees well with data from the observations (Fig. 4b). The time series of the simulated cross-shore

226   component (Fig. 4c) are virtually in phase with the observations (Fig. 4d). The magnitude of the cross-

227   shore fluctuations is comparable to the alongshore fluctuations. This is different to the anisotropic

228   characteristic of the mean currents (Fig. 3), for which the alongshore component is nearly one order of

229   magnitude larger than the cross-shore component.

230

231   Figure 4

232

233   **2.3 EOF analysis of synoptic fluctuations**

234   The Empirical Orthogonal Function (EOF) method (Emery and Thomson, 2001), as a statistical method,

235   has been used to understand synoptic fluctuations of the wintertime TWC. The simulated currents from

236   Jan. 1 to Feb. 28, 2009 were selected and their anomalies were calculated. Then, using the Matlab EOF-

237   function, the current vectors were separated into several orthogonal modes to show the spatial and

238   temporal variations. Because the first two leading modes explain 91 % of the total variance, only these

11

239   two modes were used for the analysis.

240

241   The spatial distributions of the two leading EOF modes were used to analyze the regional difference of

242   the synoptic fluctuations. To investigate the driving force of the two EOF modes, the temporal variation

243   was compared to the potential influence factors, such as wind, upstream currents, and net surface heat

244   flux.

245

246   **2.4 Momentum analysis**

247   The driving mechanisms of the synoptic fluctuations were further analyzed using the momentum

248   equation. First, the momentum balance as implemented in FVCOM (Chen et al., 2003) is shown in Eq.

249   (1). The three terms on the left hand side represent local acceleration, Coriolis acceleration, and advection,

250   respectively, and the three terms on the right hand side represent pressure gradient, friction, and diffusion,

251   respectively.

252
$$\frac{\partial \vec{V}}{\partial t} - 2\vec{\Omega} \times \vec{V} + (V \cdot \nabla \vec{V}) = -\frac{1}{\rho_0} \nabla P + \frac{\partial}{\partial z}(K_m \frac{\partial \vec{V}}{\partial z}) + \vec{F} , \qquad (1)$$

253   where $\vec{V}$ is velocity, $\vec{\Omega}$ is the Earth's rotation angular velocity, ρ_0 is the average density, P is

254   pressure, K_m is the vertical eddy viscosity coefficient, and $\vec{F}$ is horizontal diffusion.

255

256   Second, according to the hydrostatic approximation used in FVCOM [as shown in Eq. (2)], the pressure

257   gradient is given as the product of density times the gravitational acceleration. This results in Eq. (3),

258   which indicates that pressure gradient can be decomposed into the effects of the barotropic and baroclinic

259   components, as shown in Eq. (4).

$$\frac{\partial P}{\partial z} = \rho g \,, \qquad (2)$$

260

261
$$P_z = \int_z^\eta \rho g dz = \int_z^\eta (\rho_0 + \rho') g dz = \rho_0 g(z+\eta) + \int_z^\eta \rho' g dz \,, \qquad (3)$$

262
$$\nabla \vec{P} = \rho_0 g \nabla \eta + \nabla(\int_z^\eta \rho' g dz) \,, \qquad (4)$$

263 where ρ is density, ρ' is density anomaly, g is the gravitational acceleration, and η is sea surface

264 height.

265

266 Finally, the momentum equation is vertically integrated to estimate momentum balance for the water

267 column. Since the horizontal diffusion is a comparatively small term, it is neglected for simplicity.

268
$$\underbrace{\int_{-H}^0 \frac{\partial \vec{V}}{\partial t}}_{Acceleration} + \underbrace{\int_{-H}^0 -2\vec{\Omega} \times \vec{V}}_{Coriolis} + \underbrace{\int_{-H}^0 (V \cdot \nabla \vec{V})}_{Advection} = \underbrace{-gH\nabla\eta}_{Barotropic} \underbrace{- \int_{-H}^0 \nabla(\int_z^\eta \rho' g dz)}_{Baroclinic} + \underbrace{\rho_a C_D |\vec{U}|\vec{U}}_{\tau_a} \underbrace{- k_b |\vec{V_b}|\vec{V_b}}_{\tau_b} \,, \qquad (5)$$
$$\underbrace{\hphantom{-gH\nabla\eta - \int_{-H}^0 \nabla(\int_z^\eta \rho' g dz)}}_{Total\,Pr\,essure}$$

269 where τ_a is wind stress and τ_b is bottom stress, ρ_a is the density of air, $\vec{U}$ is the wind speed at 10 m

270 above sea surface, C_D is a drag coefficient at the sea surface (which varies with wind speed $\vec{U}$), k_b

271 is a bottom friction coefficient (k_b =0.005), and $\vec{V_b}$ is the simulated velocity at the bottom.

272

273 **3 Results**

274 **3.1 Mean distribution of TWC in winter**

275 Since the observational results (Su and Pan, 1987; Zeng et al., 2012) show that both branches of the

276 wintertime TWC are flowing in the subsurface, we use the vertical maximum velocity (VMV) and its

277 corresponding depth as two indices to quantify the strength of the subsurface currents (Fig. 5).

278

279 As stated above, the distribution of the VMV shows two branches of the TWC (Fig. 5a). The inshore

280   branch (Fig. 5a, blue arrow of IB), which was located between the 30 and 100 m isobaths, followed a

281   straight route from the northwest of Taiwan to the northern ECS shelf. The offshore branch (Fig. 5a, blue

282   arrow of OB) existed near the 100 m isobath and had two meanders. The two meanders turn to the cross-

283   shore direction along latitudes 26.5 °N and 28 °N. These two branches are further illustrated in the

284   distributions of current speed along the six cross-TWC sections (S1-S6), which were located at critical

285   points in the two meanders (Fig. 6). From the VMV structure, it can be inferred that the intrusions of the

286   TSC and the Kuroshio Current both affected the origin of the offshore branch (Fig. 6, S1–S3).

287

288   We further examined the subsurface current core using the depth of the VMV (Fig. 5b). We found that

289   the VMV of the TWC was located 40–60 m below the surface at the inshore branch and 20–40 m below

290   the surface at the offshore branch. Figure 6 shows the VMV positions in the subsurface layer; it also

291   illustrates that the depth of the subsurface VMV in the inshore branch was deeper than that in the offshore

292   branch. The difference can be explained by the combined effects of baroclinicity and wind friction.

293   Assuming a relatively spatially homogeneous heat loss, different cooling occurs, due to the smaller heat

294   capacity of the shallow coastal water compared to the deeper offshore waters; hence generating a

295   northwestward horizontal density gradient leading to a northeastward thermal current (vertical current

296   shear) according to the thermal wind relationship, resulting in an upward-increasing northeastward flow.

297   The northeasterly wind in winter weakens the northeastward TWC, particularly in the upper layer, which

298   leads to the formation of the subsurface VMV. Therefore, the fact that the depth of the subsurface current

299   core in the inshore branch is greater than that in the offshore branch indicates weaker baroclinicity or

300   stronger wind friction on the inshore branch than on the offshore branch.

301

302   The magnitude of the wintertime TWC was obtained by flux analysis. Two dividing lines (Fig. 5a, red

303   lines) were defined as the boundaries for the ZMCC, the TWC inshore branch, and the TWC offshore

304   branch, which had the weakest flows. The flux of each branch (Fig. 5c) was calculated using the

305   horizontal integration between the boundaries and the vertical integration in the water column. The

306   inshore branch intensifies along its way and becomes significant north of 26.5 °N, showing particularly

307   strong flow velocities between 27.5 and 28.0 °N. In this area, the subsurface current was much stronger

308   from S4 to S5 than in the other areas (Fig. 6). The flux in the entire offshore branch was large, particularly

309   north of Taiwan.

310

311   Figure 5

312

313   Figure 6

314

315   **3.2 Synoptic fluctuations**

316   The observations (Fig. 4) have demonstrated that the synoptic fluctuation in the TWC inshore branch

317   (near 121.5 °E, 27.0 °N) is significant. We further investigated the regional difference of fluctuations in

318   the two TWC branches in winter 2009 using the following three steps: (i) two regions with significant

319   fluctuations are identified by the current standard deviations of the VMV (Fig. 7) and the corresponding

320   temporal variation of vertical structures at their extremes (Fig. 8); (ii) each of the two significant

321   fluctuations is decomposed into EOF components (Fig. 9), and (iii) the influence factors, such as wind,

322   upstream currents, and net surface heat flux, are investigated by examining their correlations with the

323   first two leading EOF components (Figs. 10 and 11).

324

325 The current standard deviations (Fig. 7) shows that prominent fluctuations occurred in two regions: north

326 of Taiwan and the inshore area. The standard deviations of VMV at the two regions were larger than 0.1

327 m/s (comparable to the mean currents). In the area north of Taiwan, the fluctuation was located in the

328 origin area of the TWC offshore branch. The fluctuation in this region was in phase with the fluctuation

329 in the Taiwan Strait, indicating that the TSC played an important role in generating the fluctuation north

330 of Taiwan (to a greater extent than did the Kuroshio intrusion). The TWC fluctuation had a strong cross-

331 shore component, which means the fluctuation transported the water north of Taiwan to both the inshore

332 and offshore branches. In the inshore area, the fluctuations were influencing a wide region between the

333 30 and 100 m isobaths, with a magnitude that was sometimes larger than the mean flow (Fig. 5a). These

334 strong fluctuations led to an episodic occurrence of the TWC inshore branch, as observed at the site off

335 the Zhe-Min coast (Fig. 4, red color). When the TWC inshore branch was weakened due to these

336 fluctuations, the ZMCC might even dominate a wide region out to the 100 m isobath, especially at the

337 surface (Fig. 4, blue color).

338

339 | Figure 7 |

340

341 The vertical structures of the fluctuations north of Taiwan and in the inshore area at two representative

342 points and their relation with upper mixed layer depth are further analyzed (Fig. 8). The major component

343 (the alongshore current) of the TWC in each of the two regions (P1 and P2, Fig. 7) is used to show the

344 vertical structure of the fluctuation. The depths of the upper mixed layer were determined by a

345 Richardson number criterion (Mellor and Durbin, 1975; Grachev et al., 2013; Richardson et al., 2013),

16

346   i.e., where the critical Richardson number equals 0.25 in this paper [as in Xuan et al. (2012)]. The mean

347   depth of the upper mixed layer north of Taiwan (20 m) was much shallower than the mean depth in the

348   inshore area (42 m). However, the TWC (Fig. 8, warm color) fluctuated with significant variations of the

349   upper mixed layer depth (Fig. 8, gray lines) in both areas. When the upper mixed layer deepened, the

350   northeastward TWC (Fig. 8, warm color) was weakened or even replaced by the southwestward ZMCC,

351   and vice versa. Wind and surface cooling, which both drive the mixed layer depth, can affect the TWC

352   fluctuation.

353

354 | Figure 8 |
       | --- |

355

356   The TWC fluctuations were further decomposed into EOF modes. The first two leading EOF modes

357   account for 54% and 37% of the total variances (Fig. 9), associated with the two prominent fluctuations

358   north of Taiwan and in the inshore area (Fig. 7). Both EOF modes had a maximum fluctuation larger than

359   0.2 m/s (comparable to the mean currents). The spatial pattern of the first EOF mode (EOF1, Fig. 9a)

360   shows that the fluctuation continued from the Taiwan Strait to the area north of Taiwan, indicating that

361   the fluctuation north of Taiwan was related to the TSC and not to the Kuroshio Current. The alongshore

362   component also showed a strong fluctuation in the Taiwan Strait, which means that the TSC episodically

363   intruded the shelf. The cross-shore component revealed a fluctuation north of Taiwan that was larger than

364   0.1 m/s. This cross-shore fluctuation impacted on the trajectory of the TWS water, synoptically flowing

365   into the TWC inshore branch, offshore branch, or Kuroshio Current.

366

367   The spatial pattern of the second EOF mode (EOF2, Fig. 9b) shows a synoptic fluctuation in the inshore

368   area. The area with alongshore fluctuation (Fig. 9d) larger than 0.1 m/s was located between the 30 and

369   100 m isobaths, which demonstrates that the TWC could episodically affect this area. In addition, there

370   were cross-shore fluctuations in the inshore area (Fig. 9f), mostly along the latitudes 26.5 °N and 28 °N.

371   The latitudes of larger cross-shore fluctuations agreed well with the latitudes where the TWC offshore

372   branch of the mean currents (Fig. 5a) turned to the cross-shore direction. This indicated that the cross-

373   shore transports were most significant at the latitudes 26.5 °N and 28 °N, according to both the mean

374   currents and the synoptic fluctuations.

375

376   Figure 10 shows the temporal variation of EOF1 and its relation with north-south component of wind

377   speed, net surface heat flux, the TSC, and the Kuroshio Current. We found a close correlation between

378   EOF1 and TSC (R = 0.86), demonstrating that the TSC played the most important role in generating the

379   TWC fluctuation north of Taiwan. The EOF1 and TSC were positively correlated, meaning that a larger

380   TSC intrusion north of Taiwan leads to a cross-shore current from the coastal area to the offshore area

381   and that a weak TSC intrusion causes a cross-shore current from offshore to inshore north of Taiwan.

382

383   Figure 11 shows the temporal variation of EOF2 and its relation with the north-south component of wind

384   speed, net surface heat flux, the TSC, and the Kuroshio Current. It can be seen that EOF2 and wind are

385   well correlated (R = 0.89), indicating the important role of wind in generating the TWC fluctuation in

386   the inshore area. The northeasterly monsoon would greatly enhance the southwestward ZMCC, which

387   would then replace the northeastward TWC in the inshore area.

388

389   Figure 9

390

Figure 10

392

Figure 11

394

3.3 Dynamic diagnostics

The wintertime (January and February 2009) mean of the water column momentum balance (Fig. 12) is

used to show the overall distribution of the fundamental forces over the ECS shelf. The Coriolis force

(Fig. 12a) is mainly balanced by the total pressure (Fig. 12b) in both branches, indicating the dominant

role of geostrophic balance in the wintertime TWC. However, the wind-induced surface friction plays an

important role in the TWC, especially in the inshore area and the Taiwan Strait (Fig. 12c). The bottom

friction has an impact north of Taiwan and in the shallow Taiwan Strait, in particular when significant

Kuroshio intrusion enhances the bottom flow (Fig. 12d). The effects of advection and acceleration are

predominantly local indicated by mostly incoherent small scale distributions (Figs. 12e, 12f), so they can

be ignored when studying the large-scale current of the wintertime TWC.

405

Figure 12

407

The variation of the driving forces at two representative points P1 and P2 were used to analyze the

dynamics of synoptic fluctuations north of Taiwan and in the inshore area. Regarding the results from

the EOF analysis, the three force terms, namely Coriolis, total pressure, and wind (Fig. 13), were selected

411   to investigate the effect of the TSC on the fluctuation north of Taiwan (Fig. 9a) and the effect of wind on

412   the fluctuation in the inshore area (Fig. 9b).

413

414   In the area north of Taiwan, the cross-shore fluctuations were induced by the TSC intrusion. The variation

415   of alongshore Coriolis force (Fig. 13a, black line) was much greater than the cross-shore Coriolis force

416   (Fig. 13b, black line), which means that the fluctuation north of Taiwan was mainly in the cross-shore

417   direction. The Coriolis force (Fig. 13a, black line) was mainly balanced by the total pressure (Fig. 13a,

418   blue line), which means the currents fluctuations north of Taiwan are dominated by geostrophic balance.

419   As mentioned in Sect. 3.2, the TWC fluctuation north of Taiwan was associated with the TSC rather than

420   with the Kuroshio Current. Therefore, in the shallow coastal area the TSC mainly caused variations in

421   the depth-independent barotropic pressure gradients, which further generated the cross-shore fluctuation.

422   The mechanism can be interpreted as follows. When a larger TSC intrusion occurred, the isobaric slope

423   tilted downward from south to north, generating a cross-shore current from the coastal area to the offshore

424   area. On the contrary, when the TSC intrusion was weak, the Kuroshio intrusion from offshore to inshore

425   dominated north of Taiwan.

426

427   Wind friction (Figs. 13c and 13d) was a fundamental factor in generating the fluctuations in the inshore

428   area. Although the geostrophic balance dominated in the inshore branch for most of the time, the

429   episodically strong winter monsoon had an important role in generating the TWC fluctuations. The

430   northwestward direction Coriolis force (Fig. 13c, black line) shows that the southwestward ZMCC

431   occurred on Jan. 12, Jan. 22, and Feb. 14, 2009 and was associated with a northeasterly wind (Fig. 13c,

432   red line). It indicates that strong northeasterly monsoon in winter can reduce or even stop the

433   northeastward TWC in the inshore area, causing the intermittency of the TWC inshore branch.

434

435

Figure 13

436

437   **4 Discussion**

438   Simulated results in the winters (December-March) of the years 2010 to 2013 (Fig. 14) show that general

439   structures of the TWC in the other winters were similar to that in winter 2009 (Fig. 5 and Fig. 9), which

440   indicates that the results from the winter 2009 can be regarded as representative for the winter situation.

441   The two TWC branches and the two areas of strong fluctuations were present in all winters from 2009 to

442   2013, although their strength showed a certain inter- annual variability in accordance with the changing

443   surface forcing and boundary fluxes.

444

445

Figure 14

446

447   The wintertime TWC, which is manifested by two subsurface branches and significant synoptic

448   fluctuations, has a very different structure when compared with the stationary and surface summertime

449   TWC reported in previous studies (Guan, 1978; Fang et al., 1991; Isobe, 2008). The synoptic events,

450   with time scales of 3-15 days, play a dominant role on the horizontal advective transports. According to

451   Ledwell et al. (1998) synoptic variations are much more effective on the horizontal transport than

452   variations on shorter time scales. The synoptic fluctuations modulate the spatial structure of the

453   wintertime TWC, especially when their magnitudes are comparable with that of the mean currents, such

454   as the two prominent fluctuations north of Taiwan and in the inshore area (Fig. 7). Therefore, the two

455 prominent fluctuations will be discussed next in terms of their contributions to the alongshore and cross-

456 shore transports.

457

458 **4.1 Cross-shore transport north of Taiwan induced by the TSC**

459 In the area north of Taiwan, the TSC intrusion generated strong fluctuations of the TWC in the cross-

460 shore direction (Fig. 9a). When a larger TSC intrusion occurred, the isobaric slope tilted downward from

461 south to north, generating a cross-shore current from the coastal area to the offshore area. Compared to

462 the reported summer route that transports Taiwan Strait water to the inshore area between the 30 and 100

463 m isobaths (Guan, 1978; Fang et al., 1991; Isobe, 2008; Yang et al., 2011, 2012), our results showed that

464 most Taiwan Strait water was transported to the TWC offshore branch and to the Kuroshio area as a result

465 of the cross-shore fluctuations induced by the synoptic TSC intrusion.

466

467 A numerical tracer simulation was used to analyze the role of the cross-shore fluctuation in the transport

468 of the TSC water and the Kuroshio water north of Taiwan. In order to demonstrate the characteristics of

469 the flow patterns more clearly, artificial tracers are released in the model domain and transported by the

470 velocity field provided by the FVCOM simulation. The tracer running was part of the FVCOM simulation;

471 therefore, all the above mentioned dynamics were involved, e.g., tide, wind, and boundary forces. The

472 release location and start date of the particles were configured as follows. Two sections, one in the Taiwan

473 Strait (Fig. 15a, black dots) and another in the East Taiwan Channel (Fig. 15b, black dots), were selected

474 as the source locations for the water masses of the TSC and the Kuroshio, respectively. The particles

475 were released on January 1, 2009 and tracked until March 31, 2009 (a total of 90 days).

476

477　　Figure 15a shows the traces originating from the TSC area. Unlike the traditional route, where the TSC

478　　water flows from the Taiwan Strait to the inshore area between the 30 and 100 m isobaths, most particles

479　　(Fig. 15a, gray lines) were concentrated in the offshore branch under the effect of cross-shore fluctuation.

480　　Two particles were selected to show the inshore route (Fig. 15a, red line) and offshore route (Fig. 15a,

481　　blue line), with both passing the area north of Taiwan. When the two particles arrived at the area north

482　　of Taiwan, the behavior of the tracers, according to specific velocity conditions (Fig. 15c), was very

483　　different: a northwestward transport occurred on Jan. 25 for the inshore particles (Fig. 15c) and a

484　　northeastward transport occurred on Feb. 12 for the offshore particles (Fig. 15c). The velocity conditions

485　　in the area north of Taiwan corresponded to the variation of the Taiwan Strait flux (Fig. 10), which shows

486　　that the Taiwan Strait flux on Feb. 12 was much greater than on Jan. 25. Therefore, it can be concluded

487　　that the TSC intrusion induced an offshore transport north of Taiwan.

488

489　　Figure 15b shows the traces originating from the Kuroshio area. In the same way as the TSC water, the

490　　Kuroshio water was also transported to the northern shelf via both the inshore branch and the offshore

491　　branch. The separation of the two branches north of Taiwan was caused by cross-shore fluctuations of

492　　the currents. When the two particles arrived at the area north of Taiwan, a northwestward transport

493　　occurred on Feb. 2 for the inshore particles (Fig. 15c) and a northeastward transport occurred on Feb. 12

494　　for the offshore particles (Fig. 15c). This means that the offshore transport induced by the TSC also had

495　　an effect on the distribution of Kuroshio water north of Taiwan. Liu et al. (2016) showed that the winter

496　　TSC originated from a small branch of Kuroshio intrusion into the Luzon Strait. Our results complement

497　　this picture, since they show that most TSC particles flow into the TWC offshore branch under the

498　　influence of cross-shore fluctuation.

499

<div style="border:1px solid">

Figure 15

</div>

501

502 Our results may underestimate the impact of Kuroshio intrusion on the fluctuation of the TWC northeast

503 of Taiwan, especially at the seasonal and interannual time scales. Wei et al. (2013) demonstrated that the

504 annual and interannual variations of the Kuroshio volume transport are large. In addition, Zhou et al.

505 (2015) pointed out that the annual and interannual variations of the Kuroshio intrusion northeast of

506 Taiwan are prominent. Liu et al. (2014b) presented supportive evidence that the Kuroshio intrusion, from

507 east of Taiwan to the onshore area north of Taiwan, is closely related to the Kuroshio volume transport.

508 This relation between the Kuroshio intrusion and the Kuroshio volume transport had been interpreted by

509 Su and Pan (1987) as the β-effect because of the sudden change in topography northeast of Taiwan. Our

510 results show that the intra-seasonal variation of the Kuroshio intrusion and the Kuroshio volume transport

511 was negligible compared with the TSC variation at the same time scale, indicating that the synoptic

512 fluctuation of TWC north of Taiwan is mainly induced by the TSC. However, because FVCOM uses

513 sigma co-ordinates in the vertical which are prone to errors in regions of steep topography, our results

514 may underestimate the fluctuations at the shelf break, in particular to the northeast of Taiwan where

515 Kuroshio intrusion occurs.

516

517 **4.2 Water exchange in the inshore area induced by wind**

518 In the inshore area, the synoptic fluctuations of the TWC (Fig. 9b) caused by wind were generally strong

519 in the alongshore direction and regionally important (along the latitudes 26.5 N and 28 N) in the cross-

520 shore direction. The alongshore fluctuations showed that the TWC inshore branch occurred episodically.

24

521   This episodic occurrence of the TWC agrees with the results from a previous study based on four mooring

522   surveys off the Zhe-Min coast (Zeng et al., 2012). The mechanism of the episodic occurrence of the TWC

523   was mainly associated with the winter monsoon, which agrees with the analysis of observational data by

524   Huang et al. (2016). However, the overall magnitude of the TWC fluctuation, and its role on the cross-

525   shore flux, are still not fully understood due to the short-term nature of the observational data.

526

527   We investigated the magnitude of TWC fluctuation, and its role on the water exchange, in the inshore

528   area. Previous studies (Su and Pan, 1987; Zeng et al., 2012) show that the TWC flows between the 50

529   and 100 m isobaths, whereas the ZMCC water dominates the coastal area west of the 50 m isobath in the

530   surface layer. As mentioned when discussing Figure 9d, the strongest TWC could reach the coastal area

531   as close as the 30 m isobath, being stronger than those reported in the literature. Moreover, the area with

532   large fluctuations spanned the area between the 30 and 100 m isobaths (Fig. 9b), indicating that water

533   between the 30 and 100 m isobaths may be either ZMCC or TWC water.

534

535   The episodic occurrence of the TWC inshore branch is directly related to the relative importance of the

536   southwestward ZMCC (Fig. 16, blue arrows) and the northeastward TWC (Fig. 16, red arrows). In this

537   paper, only wind-induced synoptic fluctuations are considered, not short-term extreme storm events.

538   When the winter monsoon (the northeasterly wind) prevails, the ZMCC occupies most of the inshore

539   area and the TWC inshore branch weakens (Fig. 16a). On the contrary, the TWC inshore branch can

540   intrude into the near-coast area under southwesterly wind conditions (Fig. 16b). The boundary between

541   the coastal current and the TWC may shift from the 100 m isobaths to the 30 m isobath in the cross-shore

542   direction, covering the entire area of the TWC inshore branch.

543

544   Our results further reveal that strong wind-induced cross-shore fluctuations occur in the inshore area (Fig.

545   9f). This cross-shore fluctuation has a significant ecological impact because of the connected nutrient

546   transport (Zhao and Guo, 2011). Ren et al. (2015) observed a cross-shore flux in the inshore area, which

547   was triggered by the transition of northeasterly to southwesterly winds. Their observed features can be

548   further interpreted with our result that wind-induced fluctuations can affect the cross-shore water

549   transport in the inshore area.

550

551   Largest cross-shore fluctuations were located at the latitudes 26.5 °N and 28 °N (Fig. 9f), which agreed

552   well with the latitudes where the TWC offshore meanders occurred in the mean currents (Fig. 5a). Thus

553   the offshore transports were most significant along the latitudes 26.5 °N and 28 °N according to both the

554   mean currents and the synoptic fluctuations. The offshore transport may be associated with the offshore-

555   penetrating fronts of coastal water in the ECS. Many remote-sensing images (He et al. 2010; Bai et al.

556   2013) have exhibited offshore-penetrating fronts that crossed the 70 m isobath and played an important

557   role in cross-shore material exchange, but the mechanisms of the offshore-penetrating fronts are still

558   under debate. Yuan and Qiao (2005) pointed out that both downwelling- and upwelling-favorable winds

559   are associated with the occurrence of the offshore-penetrating front. Ren et al. (2015) suggested that the

560   penetrating front is generated by the transition of northeasterly to southwesterly winds. Wu (2015)

561   suggested that the offshore-penetrating front is the response of buoyant coastal water to an along-isobath

562   undulation of the ambient pycnocline, which is controlled by a temperature stratification of the water

563   column. Our study offers a new interpretation, i.e., that the penetrating front is generated through the

564   wind-induced fluctuations and the TWC offshore meanders.

565

566

<div style="border: 1px solid black; padding: 20px; text-align: center;">Figure 16</div>

568

5 Conclusions

The FVCOM model was able to reproduce the wintertime TWC in 2009 reasonably well, as shown by a

validation in terms of the overall structure of the surface mean currents, the ECS boundary fluxes, and

data from four mooring stations. The validation showed that the simulated TWC was comparable to the

observed results, not only in terms of the mean currents but also in terms of the synoptic fluctuations.

574

The wintertime TWC showed two branches: one inshore and another offshore. The inshore branch

covered an area between the 30 and 100 m isobaths and flowed northeastward via a straight route. The

offshore branch was located between the 100 and 200 m isobaths and showed two prominent meanders.

It was shown that the Coriolis force was nearly balanced by the pressure gradient in both branches,

indicating the dominant role of the geostrophic balance for the mean current in both branches.

580

Two regions with significant synoptic fluctuations, north of Taiwan and the inshore area, were

investigated using the EOF method. The first two leading modes explained 91% of the total variance.

EOF1 showed that fluctuations occurred in the cross-shore direction south of 26 N. These fluctuations

were mainly associated with variation of the TSC flux. EOF2 showed significant fluctuation between the

30 and 100 m isobaths. These fluctuations caused the episodic existence of the TWC inshore branch in

the alongshore direction and cross-shore fluctuations mainly at latitudes 26.5 N and 28 N, which were

27

587 mainly associated with the variation of wind speed.

588

589 We also studied the different dynamic reasons for the fluctuations in the two regions. In the area north of

590 Taiwan, the TSC and Kuroshio converged to initiate the TWC. A barotropic pressure anomaly was

591 generated by TSC intrusion from the Taiwan Strait causing a barotropic pressure gradient in the

592 alongshore direction; this explains why the synoptic fluctuations in this area occurred in the cross-shore

593 direction. Additionally, the wind had a strong effect on the synoptic fluctuations in the inshore area. The

594 northeasterly monsoon enhanced the southwestward ZMCC and replaced the TWC in the inshore area.

595 This situation is reversed during the southwesterly wind.

596

597 The synoptic fluctuations north of Taiwan and in the inshore area are important for both the alongshore

598 and cross-shore transports. Due to the fluctuation north of Taiwan, the mixed water of the TSC and the

599 Kuroshio was transported to both the inshore area and the offshore area, whereas most Taiwan Strait

600 water was transported to the offshore area in winter. The inshore fluctuation not only caused an episodic

601 occurrence of the TWC in the alongshore direction, which affected the alongshore transport of ZMCC

602 water and TWC water between the 30 and 100 m isobaths, but also impacted the cross-shore transports

603 along latitudes 26.5 $^\circ$N and 28 $^\circ$N.

604

605 **Acknowledgement**

613

614   **References**

615

616   Bai, Y., Pan, D., Cai, W. J., He, X., Wang, D., Tao, B., and Zhu, Q.: Remote sensing of salinity from
617   satellite-derived CDOM in the Changjiang River dominated East China Sea, J. Geophys. Res. Ocean,
618   118, 227–243, 2013.

619   Bleck, R.: An oceanic general circulation model framed in hybrid isopycnic-Cartesian coordinates,
620   Ocean Model., 37, 55–88, 2002.

621   Brink, K. H.: Costal trapped waves and wind-induced currents over the continental shelf, Annual Review
622   of Fluid Mechanics, 23, 389-412, 1991.

623   Carnes, M. R.: Description and evaluation of GDEM-V3.0, NRL Rep. NRL/MR/7330-09-9165, Nav.
624   Res. Lab., Washington, D. C, 2009.

625   Chen, C., Liu, H., and Beardsley, R. C.: An unstructured, finite-volume, three-dimensional, primitive
626   equation ocean model: application to coastal ocean and estuaries, J. Atm. Oceanic Tech., 20, 159–
627   186, 2003.

628   Chen, C., Beardsley, R. C., Limeburner, R., and Kim, K.: Comparison of winter and summer
629   hydrographic observations in the Yellow and East China seas and adjacent Kuroshio during 1986,
630   Cont. Shelf Res., 14, 909–929, 1994.

631   Chen, C., Xue, P., Ding, P., Beardsley, R. C., Xu, Q., Mao, X., Gao, G., Qi, J., Li, C., Lin, H., Cowles,
632   G., and Shi, M.: Physical mechanisms for the offshore detachment of Changjiang Diluted Water in
633   the East China Sea, J. Geophys. Res., 113, C02002, doi:10.1029/2006JC003994, 2008.

634   Chen, C. T. A. and Wang, S. L.: Carbon, alkalinity and nutrient budget on the East China Sea continental
635   shelf, J. Geophys. Res. Ocean, 104, 20675–20686, 1999.

636   Chuang, W. S. and Liang, W. D.: Seasonal variability of intrusion of the Kuroshio water across the
637   continental shelf northeast of Taiwan, J. Oceanogr., 50(5), 531–542, 1994.

638   Cui, M., Hu, D., and Wu, L.: Seasonal and intraseasonal variations of the surface Taiwan Warm Current,
639   Chin. J. Oceanol. Limnol., 22, 271–277, 2004.

640   Egbert, G. D., Bennett, A., and Foreman, M.: TOPEX/Poseidon tides estimated using a global inverse
641   model, J. Geophys. Res. 99, 24821–24852, doi: 10.1029/94JC01894, 1994.

642   Egbert, G. D. and Erofeeva, S. Y.: Efficient inverse modeling of barotropic ocean tides, J. Atmos. Oceanic
643   Technol., 19, 183–204, 2002.

644   Emery, W. J. and Thomson, R. E.: Data analysis methods in physical oceanography, Second and revised
645   version, 658 pp., Elsevier Science B.V., Ameterdam, The Netherland, 2001.

646   Fang, G., Zhao, B., and Zhu, Y.: Water volume transport through the Taiwan Strait and the continental

shelf of the East China Sea measured with current meters, in Oceanography of Asian Marginal Seas, edited by K. Takano, 345–358pp., doi:10.1016/S0422-9894(08)70107-7, Elsevier, New York, 1991.

Feng, M., Mitsudera, H., and Yoshikawa, Y.: Structure and Variability of the Kuroshio Current in Tokara Strait, J. Phys. Oceanogr., 30(9), 2257–2276, 2000.

Godin, G.: The Analysis of Tides, 264 pp., University of Toronto Press, Toronto, 1972.

Grachev, A. A., Andreas, E. L., Fairall, C. W., Guest, P. S., and Persson, P. O. G.: The critical Richardson number and limits of applicability of local similarity theory in the stable boundary layer, Boundary-layer meteorology, 147(1), 51–82, 2013.

Guan, B. and Fang, G.: Winter counter-wind currents off the southeastern China coast: A review, J. Oceanogr., 62, 1–24, 2006.

Guan, B. and Mao, H.: A note on circulation of the East China Sea, Chin. J. Oceanol. Limnol., 1, 5–16, 1982.

Guan, B. X.: A sketch of the current system of the East China Sea, in Collected Papers of the Continental Shelf of the East China Sea (in Chinese), 126–133pp., Inst. of Oceanol., Chin. Acad. of Sci., Qingdao, China, 1978.

Guo, X. Y., Hukuda, H., Miyazawa, Y., and Yamagata, T.: A triply nested ocean model for simulating the Kuroshio - Roles of horizontal resolution on JEBAR, J. Phys. Oceanogr., 33, 146–169, 2003.

Guo, X. Y., Miyazawa, Y., and Yamagata, T.: The Kuroshio onshore intrusion along the shelf break of the East China Sea: The origin of the Tsushima Warm Current, J. Phys. Oceanogr., 36, 2205–2231, doi:10.1175/JPO2976.1, 2006.

He, L., Li, Y., Zhou, H., and Yuan, D.: Variability of cross-shelf penetrating fronts in the East China Sea, Deep Sea Res., 57, 1820–1826, 2010.

Hong, H., Chai, F., Zhang, C., Huang, B., Jiang, Y., and Hu, J.: An overview of physical and biogeochemical processes and ecosystem dynamics in the Taiwan Strait, Cont. Shelf Res., 31, 3-12, 2011.

Hsin, Y. C., Qiu, B., Chiang, T. L., and Wu, C. R.: Seasonal to interannual variations in the intensity and central position of the surface Kuroshio east of Taiwan, J. Geophys. Res. Oceans, 118(9), 4305–4316, 2013.

Hu, J., Kawamura, H., Li, C., Hong, H., and Jiang, Y.: Review on current and seawater volume transport through the Taiwan Strait, J. Oceanogr., 66, 591-610, 2010.

Huang, D., Zeng, D., Ni, X., Zhang, T., Xuan, J., Zhou, F., Li, J., and He, S.: Alongshore and cross-shore circulations and their response to winter monsoon in the western East China Sea, Deep-Sea Res. II, 124, 6–18, http://dx.doi.org/10.1016/j.dsr2.2015.01.001i, 2016,

Hung, J. J., Chen, C. H., Gong, G. C., Sheu, D. D., and Shiah, F. K.: Distributions, stoichiometric patterns and cross-shelf exports of dissolved organic matter in the East China Sea, Deep-Sea Res. II, 50, 1127–1145, 2003.

Huthnance, J. M., Mysak, L. A., and Wang, D. P.: Coastal trapped waves, in: Mooers C.N.K. (ed.) Baroclinic Processes on Continental Shelves. Coastal and Estuarine Sciences, 3, pp. 1-18. Washington DC, American Geophysical Union, 1986.

Huyer, A.: Shelf circulation, In Mehaute, B. L., Hames, D. M. (Eds.), The Sea, Volume 9: Ocean Engineering Science, Wiley, pp. 423–466, 1990.

Isobe, A.: Recent advances in ocean-circulation research on the Yellow Sea and East China Sea shelves, J. Oceanogr., 64, 569–584, doi:10.1007/s10872-008-0048-7, 2008.

Johns, W. E., Lee, T. N., Zhang, D., Zantopp, R., Liu, C. T., and Yang, Y.: The Kuroshio east of Taiwan:

691   Moored transport observations from the WOCE PCM-1 array, J. Phys. Oceanogr., 31(4), 1031–1053,
692   2001.

693   Ledwell, J. R., Watson, A. J., and Law, C. S.: Mixing of a tracer in the pycnocline, J. Geophys. Res.,
694   103(C10), 21499–21529, doi:10.1029/98JC01738, 1998.

695   Lee, J. S. and Matsuno, T.: Intrusion of Kuroshio water onto the continental shelf of the East China Sea,
696   J. Oceanogr., 63, 309–325, 2007.

697   Liu, C., Wang, F., Chen, X., and VonStorch, J. S.: Interannual variability of the Kuroshio onshore
698   intrusion along the East China Sea shelf break: Effect of the Kuroshio volume transport, J. Geophys.
699   Res. Oceans, 119, 6190–6209, doi:10.1002/2013JC009653, 2014a.

700   Liu, T., Xu, J., He, Y., Lü, H., Yao, Y., and Cai, S.: Numerical simulation of the Kuroshio intrusion into
701   the South China Sea by a passive tracer, Acta Oceanologica Sinica, 35(9): 1–12, doi:
702   10.1007/s13131-016-0930-x, 2016.

703   Liu, X., Dong, C., Chen, D., and Su, J.: The pattern and variability of winter Kuroshio intrusion northeast
704   of Taiwan, J. Geophys. Res. Oceans, 119, 5380–5394, DOI 10.1002/2014JC009879, 2014b.

705   Mellor, G. L. and Durbin, P A.: The structure and dynamics of the ocean surface mixed layer, J. Phys.
706   Oceanogr., 5(4), 718–728, 1975.

707   Oey, L. Y., Hsin, Y. C., and Wu, C. R.: Why does the Kuroshio northeast of Taiwan shift shelfward in
708   winter?, Ocean Dynam., 60(2), 413–426, 2010.

709   Qiu, B. and Imasato, N.: A numerical study on the formation of the Kuroshio countercurrent and the
710   Kuroshio Branch Current in the East China Sea, Cont. Shelf Res., 10, 165–184, doi:10.1016/0278-
711   4343(90)90028-K, 1990.

712   Ren, J. L., Xuan, J., Wang, Z. W., Huang, D., and Zhang, J.: Cross-shelf transport of terrestrial Al
713   enhanced by the transition of northeasterly to southwesterly monsoon wind over the East China Sea,
714   J. Geophys. Res. Oceans, 120, doi:10.1002/2014JC010655, 2015.

715   Richardson, H., Basu, S., and Holtslag, A. A. M.: Improving stable boundary-layer height estimation
716   using a stability-dependent critical bulk Richardson number, Boundary-layer meteorology, 148(1),
717   93–109, 2013.

718   Smith, W. H. F. and Sandwell, D. T.: Global sea floor topography from satellite altimetry and ship depth
719   soundings, Science, 277, 1956–1962, 1997.

720   Su, J. L. and Pan, Y. Q.: On the shelf circulation north of Taiwan, Acta Oceanol. Sin., 6, 1–20, 1987.

721   Su, J. L., Pan, Y. Q., and Liang, X. S.: Kuroshio intrusion and Taiwan warm current, Oceanology of
722   China Seas. Springer Netherlands, 59–70, 1994.

723   Takahashi, D. and Morimoto, A.: Mean field and annual variation of surface flow in the East China Sea
724   as revealed by combining satellite altimeter and drifter data, Prog. Oceanogr., 111, 125–139, doi:
725   10.1016/j.pocean.2013.01.007, 2013.

726   Teague, W., Jacobs, G., Ko, D., Tang, T., Chang, K. I., and Suk, M. S.: Connectivity of the Taiwan, Cheju,
727   and Korea straits, Conti. Shelf Res., 23(1), 63–77, 2003.

728   Uppala, S. M., KÅllberg, P. W., Simmons, A. J., Andrae, U., Bechtold, V. D. C., Fiorino, M., Gibson, J.
729   K., Haseler, J., Hernandez, A., Kelly, G. A., Li, X., Onogi, K., Saarinen, S., Sokka, N., Allan, R. P.,
730   Andersson, E., Arpe, K., Balmaseda, M. A., Beljaars, A. C. M., Berg, L. V. D., Bidlot, J., Bormann,
731   N., Caires, S., Chevallier, F., Dethof, A., Dragosavac, M., Fisher, M., Fuentes, M., Hagemann, S.,
732   Hólm, E., Hoskins, B. J., Isaksen, L., Janssen, P. A. E. M., Jenne, R., Mcnally, A. P., Mahfouf, J.-F.,
733   Morcrette, J.-J., Rayner, N. A., Saunders, R. W., Simon, P., Sterl, A., Trenberth, K. E., Untch, A.,
734   Vasiljevic, D., Viterbo, P., and Woollen, J.: The ERA-40 re-analysis, Q. J. R. Meteorol. Soc., 131,

735   2961–3012. doi:10.1256/qj.04.176, 2005.

736   Wang, Y., Jan, S., and Wang, D.: Transports and tidal current estimates in the Taiwan Strait from
737   shipboard ADCP observations (1999–2001), Estuarine Coastal Shelf Sci., 57(1), 193–199, 2003.

738   Wei, Y., Huang, D., and Zhu, X. H.: Interannual to decadal variability of the Kuroshio Current in the east
739   china sea from 1955 to 2010 as indicated by in-situ hydrographic data, J. Oceanogr., 69(5), 571–
740   589, 2013.

741   Wu, H.: Cross-shelf penetrating fronts: A response of buoyant coastal water to ambient pycnocline
742   undulation, J. Geophys. Res., 120, doi:10.1002/2014JC010686, 2015.

743   Wu, C. R. and Hsin, Y. C.: Volume transport through the Taiwan Strait: a numerical study, Terr. Atmos.
744   Ocean. Sci., 16(2), 377–391, 2005.

745   Xuan, J., Huang, D., Zhou, F., Zhu, X. H., and Fan, X.: The role of wind on the detachment of low salinity
746   water in the Changjiang Bank in summer, J. Geophys. Res. Ocean, 117, C10004, doi:
747   10.1029/2012JC008121, 2012.

748   Xuan, J., Yang, Z., Huang, D., Wang, T., and Zhou, F.: Tidal residual current and its role in the mean flow
749   on the Changjiang Bank, J. Mar. Syst., 154, 66–81, doi: 10.1016/j.jmarsys.2015.04.005, 2016.

750   Xuan, J., Zhou, F., Huang, D., Zhu, X. H., Xing, C., and Fan, X.: Modelling the timing of major spring
751   bloom events in the central Yellow Sea, Estuarine Coastal Shelf Sci., 113, 283–292, 2012.

752   Yang, D., Yin, B., Liu, Z., and Feng, X.: Numerical study of the ocean circulation on the East China Sea
753   shelf and a Kuroshio bottom branch northeast of Taiwan in summer, J. Geophys. Res. Ocean, 116,
754   C05015, doi:10.1029/2010JC006777, 2011.

755   Yang, D., Yin, B., Liu, Z., Bai, T., Qi, J., and Chen, H.: Numerical study on the pattern and origins of
756   Kuroshio branches in the bottom water of southern East China Sea in summer, J. Geophys. Res.
757   Ocean, 117, C02014, doi:10.1029/2011JC007528, 2012.

758   Yu, L. and Weller, R. A.: Objectively Analyzed air–sea heat Fluxes (OAFlux) for the global oceans, B.
759   Am. Meteorol. Soc. 88, 527–539, 2007.

760   Yuan, D., Qiao, F., and Su, J.: Cross-shelf penetrating fronts off the southeast coast of China observed by
761   MODIS. Geophys. Res. Lett., 32, L19603, doi:10.1029/2005GL023815, 2005.

762   Zeng, D. Y., Ni, X., and Huang, D.: Temporal and spatial variability of the Zhe-Min Coastal Current and
763   the Taiwan Warm Current in winter in the southern Zhejiang coastal sea, Sci. Sin. Terrae., 42, 1123–
764   1134, 2012.

765   Zhao, L. and Guo, X.: Influence of cross-shelf water transport on nutrients and phytoplankton in the East
766   China Sea: A model study, Ocean Sci., 7, 27–43, doi:10.5194/os-7–27-2011, 2011.

767   Zhou, F., Xue, H., Huang, D., Xuan, J., Ni, X., Xiu, P., and Hao, Q.: Cross shelf exchange in the shelf of
768   the East China Sea, J. Geophys. Res. Oceans, 120, 1545–1572, doi:10.1002/2014JC010567, 2015.

769   Zhu, J., Chen, C., Ding, P., Li, C., and Lin, H.: Does the Taiwan Warm Current exist in winter?, Geophys.
770   Res. Lett., 31, L12302, doi:10.1029/2004GL019997, 2004.

771   **Table Captions**

772   Table 1: Annual-mean volume transports (Sv = 10^6 m^3/s) through various sections. The sections are

773   shown in Figure 2 using blue dashed lines.

774

Figure Captions

Figure 1: Density (σ_t, kg/m^3) distributions at 50 m depth derived from the GDEM climatological data in February (a), an ocean survey from Feb. 1–27, 2007 (b), and an ocean survey from Feb. 3–16, 2007 (c), with the density anomalies between the GDEM data and the two surveys (d and e). The two blue arrows indicate the two TWC branches in winter. The 30, 50, 70, 100 and 200 m isobaths are indicated with grey lines in panel a.

Figure 2: The FVCOM model grid (Left) and the surface mean flow in the ECS in winter (Right). The colors in the left panel show the grid length (km). The letters a, b, and c indicate the three open boundaries at the Taiwan Strait, the northwest Pacific Ocean, and the Japan/East Sea, respectively. The blue dashed lines (right) show some important straits around shelf boundary, including the Taiwan Strait (TWS), the East Taiwan Channel (ET), the Tsushima Strait (TUS), the Tokara Strait (TOS), and shelf break at the 200 m isobath. The red rectangle shows the study area of the wintertime TWC. The four red numbers off the Zhe-Min coast shows the four mooring sites observed from Jan. 5 to Feb. 28, 2009.

Figure 3: Validations of the wintertime TWC (warm color) along the section off the Zhe-Min coast (the short line with four red numbers in Figure 2): (a) observed alongshore currents; (b) simulated alongshore currents; (c) observed cross-shore currents; (d) simulated cross-shore currents. Note, an enlarged color scale is used for the cross-shore component to have a clear view of its weak structure.

Figure 4: Validations of the wintertime TWC fluctuations: (a) observed alongshore currents; (b) simulated alongshore currents; (c) observed cross-shore currents; (d) simulated cross-shore currents. The

797   observation data comes from Station 4 in Figure 1 and the simulated data has the same position and

798   period as the observation data.

799

800   Figure 5: a) Distribution of flow axes in the ECS in winter. The black arrows show the maximum velocity

801   (m/s) in the vertical profile (VMV) and the color shows the speed of the VMV. The two blue arrows with

802   label IB and OB represent the flow axes of the inshore branch and offshore branch, respectively. The red

803   line DL1 represents the dividing line between the coastal current and inshore branch, and the red line

804   DL2 separates the two TWC branches. b) Depth (m) of flow axes in the ECS, shown by color. Sections

805   S1–S6 were selected to study the wintertime TWC. c) Flux of inshore branch (blue) and offshore branch

806   (red) at different latitudes. Dashed lines show the positions of Sections. S1–S6. Note, the scale is not

807   linear.

808

809   Figure 6: Distributions of current speed along the six sections S1–S6 in winter. The blue arrow on the

810   left indicates the inshore branch according to the velocity cores from section S3 to S6. The blue arrow

811   on the right indicates the offshore branch according to the velocity cores from section S2 to S6. TSC is

812   the Taiwan Strait Warm Current.

813

814   Figure 7: Current standard deviation in the layer of the VMV. The black arrows indicate the major axis

815   of the ellipse which represent the standard deviation of the current. The color shading shows the

816   respective magnitude. The two blue arrows indicate the two TWC branches. The red curve indicate the

817   area where the current standard deviation is larger than 0.1 m/s and the branches' representative points

818   (P1 and P2) are selected for later analysis.

819

Figure 8: Variation of alongshore currents (m/s, shown by color scale) for the entire water column north

of Taiwan (P1) and in the inshore area (P2) and their relation with upper mixed layer depth. The positive

velocity (warm color) indicates the occurrence of the TWC. The gray solid lines show the depth of the

upper mixed layer.

824

Figure 9: The spatial pattern of the first (EOF1; left) and second (EOF2; right) leading modes of the

VMV in the ECS: (a) EOF1 currents, (b) EOF2 currents, (c) EOF1 alongshore component, (d) EOF2

alongshore component, (e) EOF1 cross-shore component, and (f) EOF2 cross-shore component (all

shown by black arrows with the color representing the magnitude). The 30, 50, 70, 100 and 200 m

isobaths are indicated with grey lines.

830

Figure 10: Temporal variation of EOF1, north-south component of wind speed, surface net heat flux, and

TSC flux across the TWS section, and Kuroshio flux across the ET section. Their linear correlation

coefficients R and time-lags are also indicated in each panel. The p value is a declining indicator which

indicates the impact significance of the linear correlation coefficients R whereby R has statistical

significance and the confidence level is larger than 95% when the p value is less than 0.05.

836

Figure 11: Temporal variation of EOF2, north-south component of wind speed, surface net heat flux, and

TSC flux across the TWS section, and Kuroshio flux across the ET section. Their linear correlation

coefficients and time-lags are also indicated in each panel.

840

841   Figure 12: The effects of Coriolis force (a), total pressure (b), surface friction (c), bottom friction (d),

842   advection (e), and local acceleration (f) for water column in winter according to Eq. (5) (shown by black

843   arrows with the color representing the magnitude; units: 10^{-4} m^2/s^2). The two blue arrows indicate the

844   two TWC branches. The two triangles indicate the two regions with significant fluctuation north of

845   Taiwan (P1) and in the inshore area (P2).

846

847   Figure 13: Variations in Coriolis force, total pressure, and wind in the cross-shore direction at P1 (a), the

848   alongshore direction at P1 (b), the cross-shore direction at P2 (c), and the alongshore direction at P2 (d)

849   according to Eq. (5). The grey pointers indicate the alongshore and cross-shore directions of dynamical

850   effects in the earth coordinate system.

851

852   Figure 14: Mean currents (upper panels) and synoptic fluctuations (EOF1 in middle panels and EOF2 in

853   bottom panels) in winters of 2010-2013. The black arrows in the upper panels show the velocity (m/s) in

854   the layer of VMV with the color representing the current speed. The two blue arrows with label IB and

855   OB represent the flow axes of the inshore branch and offshore branch, respectively. The black arrows in

856   the middle panels and bottom panels represent the EOF components (m/s) with their magnitude

857   represented by color scales.

858

859   Figure 15: Traces of TSC water (a) and Kuroshio water (b) in winter, with the variation of surface currents

860   north of Taiwan (c). The green lines L1 and L2 indicate the starting latitude of the tracers (24.5 °N) and

861   the latitude which is representative for synoptic fluctuations north of Taiwan (25.8 °N), respectively. The

862   black dots represent the release locations of tracers originated from line L1. The gray lines show the

863   entire trajectories of the tracers. The red lines and blue lines are selected trajectories, which are close to

864   the inshore branch and offshore branch, respectively. The dates show the times when selected tracers

865   cross the latitude indicated by line L2. The numbers are the depths of the tracers, which are labeled at an

866   interval of six days. The two black arrows represent the two TWC branches.

867

868   Figure 16: The VMV under the northerly wind (a) and southerly wind (b). Panel (c) shows the variation

869   of wind in winter. Blue vectors and red vectors show the southwestward coastal current and the

870   northeastward TWC, respectively. Gray contours indicate the 30, 50, 70, and 100 m isobaths. The two

871   black arrows represent the two TWC branches. The green ellipse indicates the inshore area with

872   significant fluctuation.

873

Table 1: Annual-mean volume transports (Sv $= 10^6$ m^3/s) through various sections. The sections are

shown in Figure 2 using blue dashed lines.

Section	Present model	Previous estimates
Taiwan Strait	1.22	1.2 (Isobe, 2008)
		1.8 (Wang et al., 2003)
		1.09 (Wu and hsin, 2005)
		1.03 (Yang et al., 2011)
		1.72 (Guo et al., 2006)
		0.5 (Hung et al., 2003)
		1.10 (Liu et al., 2014b)
Tsushima Strait	2.85	2.65 (Isobe, 2008)
		3.03 (Guo et al., 2006)
		2.70 (Yang et al., 2011)
		2.52 (Liu et al., 2014b)
200m isobath	1.66	1.46 (Guo et al., 2006)
		0.87 (Liu et al., 2014a)
		3.0 (Teague et al., 2003)
		2.74 (Lee and Matsuno, 2007)
East Taiwan Channel	22.71	21.50 (Johns et al., 2001)
		23.00 (Teague et al., 2003)
		23.83 (Guo et al., 2006)
		28.4 (Hsin et al., 2013)
		21.37 (Yang et al., 2011)
		20.74 (Liu et al., 2014b)
Tokara Strait	23.20	23.4 (Feng et al., 2000)
		20.00 (Teague et al., 2003)
		20.66 (Yang et al., 2011)
		24.42 (Liu et al., 2014b)
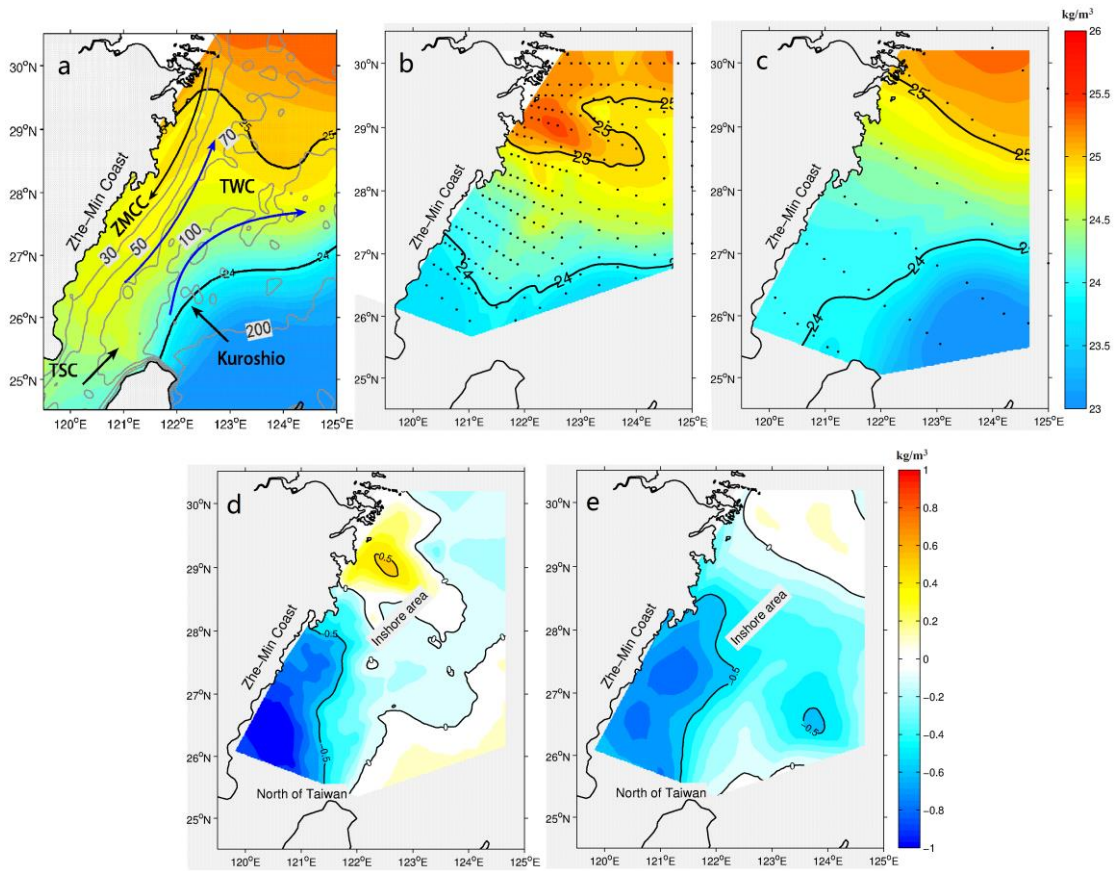
880 Figure 1: Density (σ_t, kg/m³) distributions at 50 m depth derived from the GDEM climatological data in

881 February (a), an ocean survey from Feb. 1–27, 2007 (b), and an ocean survey from Feb. 3–16, 2007 (c),

882 with the density anomalies between the GDEM data and the two surveys (d and e). The two blue arrows

883 indicate the two TWC branches in winter. The 30, 50, 70, 100 and 200 m isobaths are indicated with grey

884 lines in panel a.

885

Figure 2: The FVCOM model grid (Left) and the surface mean flow in the ECS in winter (Right). The colors in the left panel show the grid length (km). The letters a, b, and c indicate the three open boundaries at the Taiwan Strait, the northwest Pacific Ocean, and the Japan/East Sea, respectively. The blue dashed lines (right) show some important straits around shelf boundary, including the Taiwan Strait (TWS), the East Taiwan Channel (ET), the Tsushima Strait (TUS), the Tokara Strait (TOS), and shelf break at the 200 m isobath. The red rectangle shows the study area of the wintertime TWC. The four red numbers off the Zhe-Min coast shows the four mooring sites observed from Jan. 5 to Feb. 28, 2009.

895

896 Figure 3: Validations of the wintertime TWC (warm color) along the section off the Zhe-Min coast (the

897 short line with four red numbers in Figure 2): (a) observed alongshore currents; (b) simulated alongshore

898 currents; (c) observed cross-shore currents; (d) simulated cross-shore currents. Note, an enlarged color

899 scale is used for the cross-shore component to have a clear view of its weak structure.

900
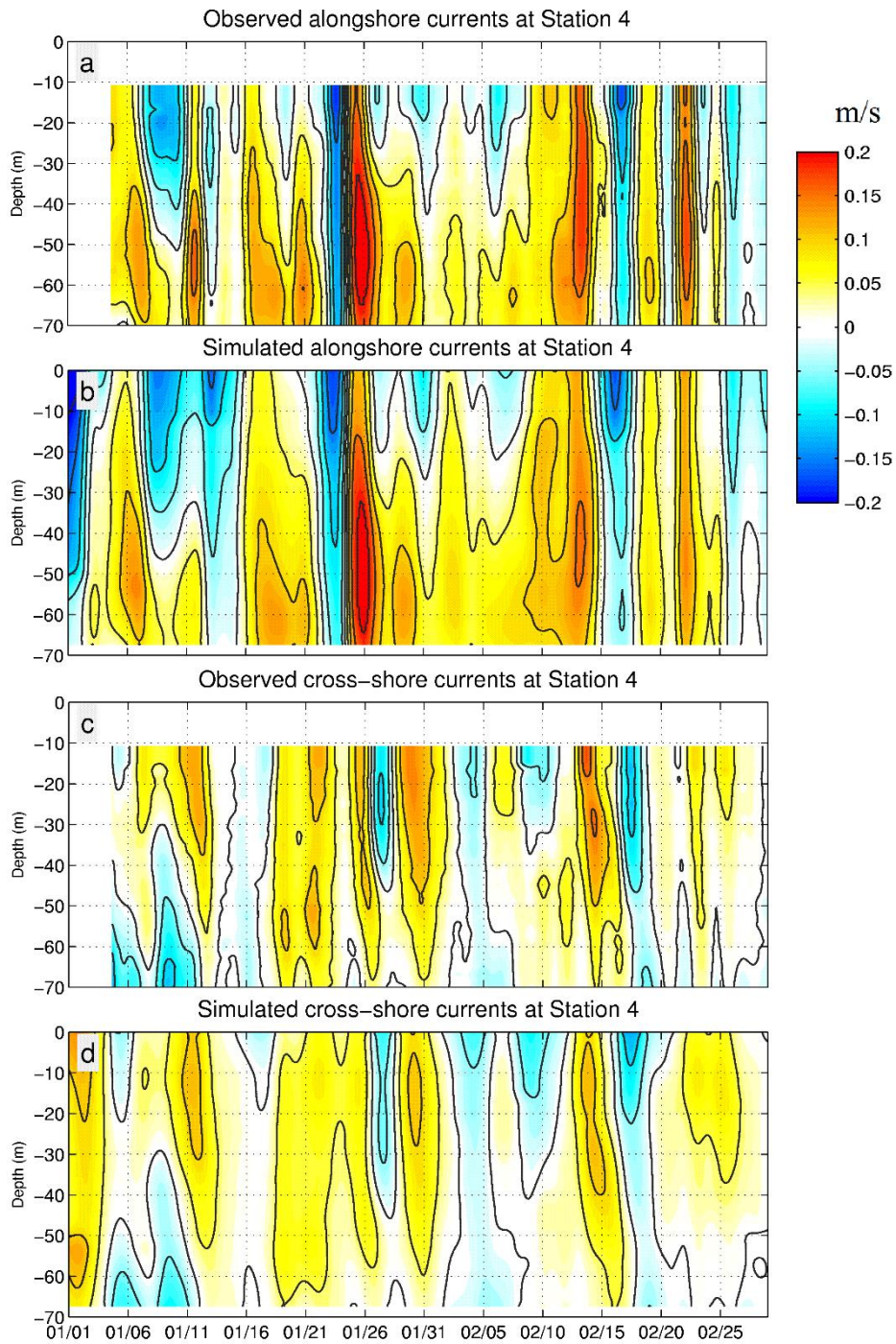
Figure 4: Variations of the inshore branch of TWC during January and February 2009: (a) observed alongshore currents; (b) simulated alongshore currents; (c) observed cross-shore currents; (d) simulated cross-shore currents. The observation data comes from Station 4 in Figure 1 and the simulated data has the same position and period as the observation data.

907

Figure 5: a) Distribution of flow axes in the ECS in winter. The black arrows show the maximum velocity

(m/s) in the vertical profile (VMV) and the color shows the speed of the VMV. The two blue arrows with

label IB and OB represent the flow axes of the inshore branch and offshore branch, respectively. The red

line DL1 represents the dividing line between the coastal current and inshore branch, and the red line

DL2 separates the two TWC branches. b) Depth (m) of flow axes in the ECS, shown by color. Sections

S1–S6 were selected to study the wintertime TWC. c) Flux of inshore branch (blue) and offshore branch

(red) at different latitudes. Dashed lines show the positions of Sections. S1–S6. Note, the scale is not

linear.

917

Figure 6: Distributions of current speed along the six sections S1–S6 in winter. The blue arrow on the

left indicates the inshore branch according to the velocity cores from section S3 to S6. The blue arrow

on the right indicates the offshore branch according to the velocity cores from section S2 to S6. TSC is

the Taiwan Strait Current.

922

Figure 7: Current standard deviation in the layer of the VMV. The black arrows indicate the major axis of the ellipse which represent the standard deviation of the current. The color shading shows the respective magnitude. The two blue arrows indicate the two TWC branches. The red curve indicate the area where the current standard deviation is larger than 0.1 m/s and the branches' representative points (P1 and P2) are selected for later analysis.

930

Figure 8: Variation of alongshore currents (m/s, shown by color scale) for the entire water column north

of Taiwan (P1) and in the inshore area (P2) and their relation with upper mixed layer depth. The positive

velocity (warm color) indicates the occurrence of the TWC. The gray solid lines show the depth of the

upper mixed layer.

935

936

Figure 9: The spatial pattern of the first (EOF1; left) and second (EOF2; right) leading modes of the

VMV in the ECS: (a) EOF1 currents, (b) EOF2 currents, (c) EOF1 alongshore component, (d) EOF2

alongshore component, (e) EOF1 cross-shore component, and (f) EOF2 cross-shore component (all

shown by black arrows with the color representing the magnitude). The 30, 50, 70, 100 and 200 m

isobaths are indicated with grey lines.

942

943

Figure 10: Temporal variation of EOF1, north-south component of wind speed, surface net heat flux, and

TSC flux across the TWS section, and Kuroshio flux across the ET section. Their linear correlation

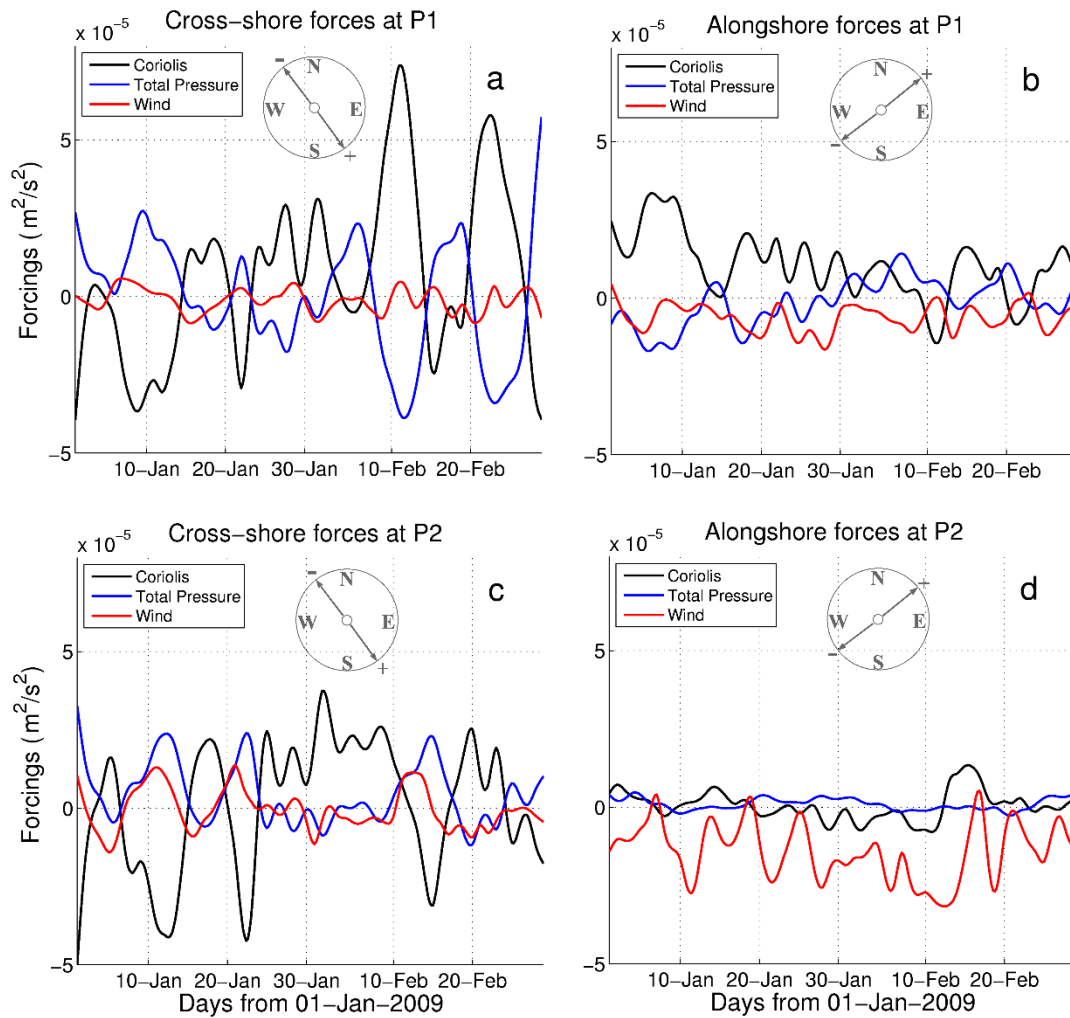coefficients R and time-lags are also indicated in each panel. The p value is a declining indicator which

indicates the impact significance of the linear correlation coefficients R whereby R has statistical

significance and the confidence level is larger than 95% when the p value is less than 0.05.

950

Figure 11: Temporal variation of EOF2, north-south component of wind speed, surface net heat flux, and

TSC flux across the TWS section, and Kuroshio flux across the ET section. Their linear correlation

coefficients and time-lags are also indicated in each panel.

955

Figure 12: The effects of Coriolis force (a), total pressure (b), surface friction (c), bottom friction (d),

advection (e), and local acceleration (f) for water column in winter according to Eq. (5) (shown by black

arrows with the color representing the magnitude; units: 10^{-4} m^2/s^2). The two blue arrows indicate the

two TWC branches. The two triangles indicate the two regions with significant fluctuation north of
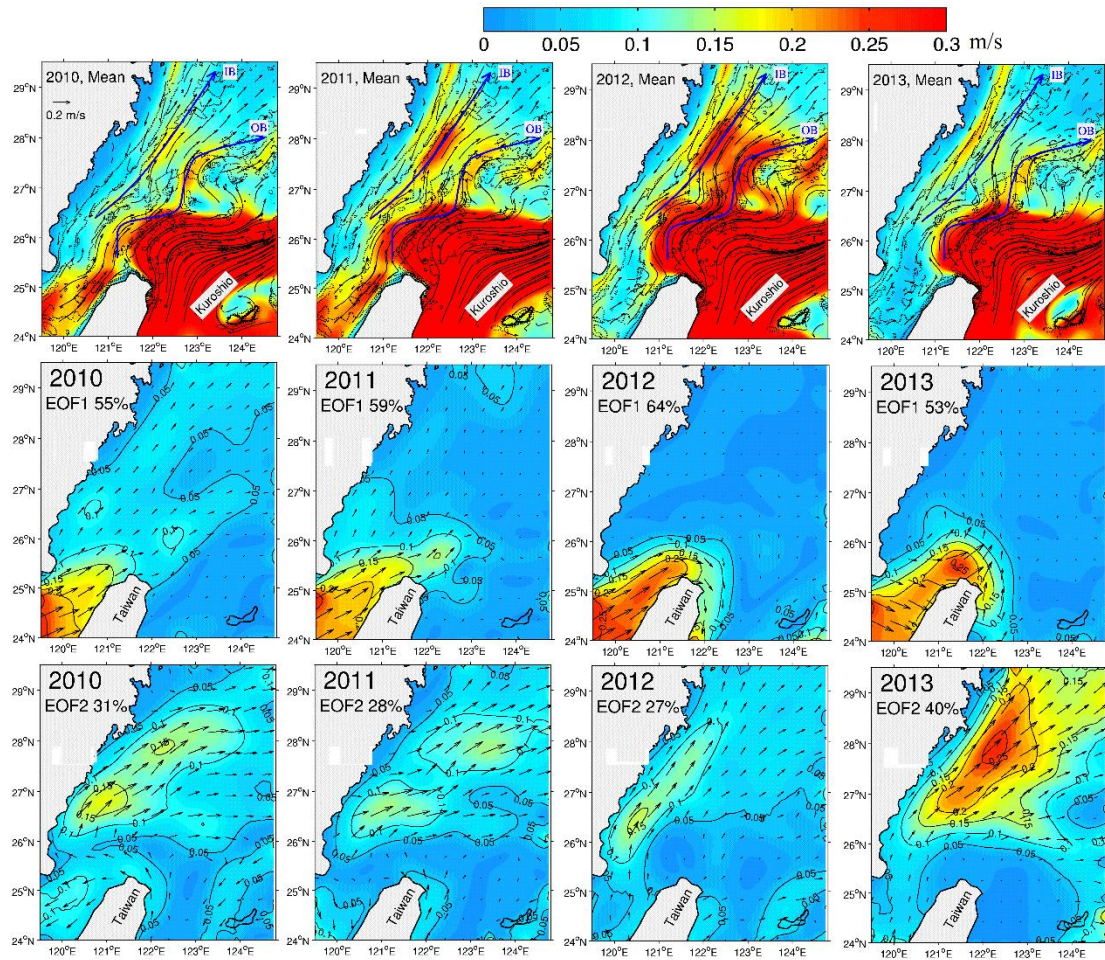
Taiwan (P1) and in the inshore area (P2).

961

962

Figure 13: Variations in Coriolis force, total pressure, and wind in the cross-shore direction at P1 (a), the

alongshore direction at P1 (b), the cross-shore direction at P2 (c), and the alongshore direction at P2 (d)

according to Eq. (5). The grey pointers indicate the alongshore and cross-shore directions of dynamical

effects in the earth coordinate system.

963
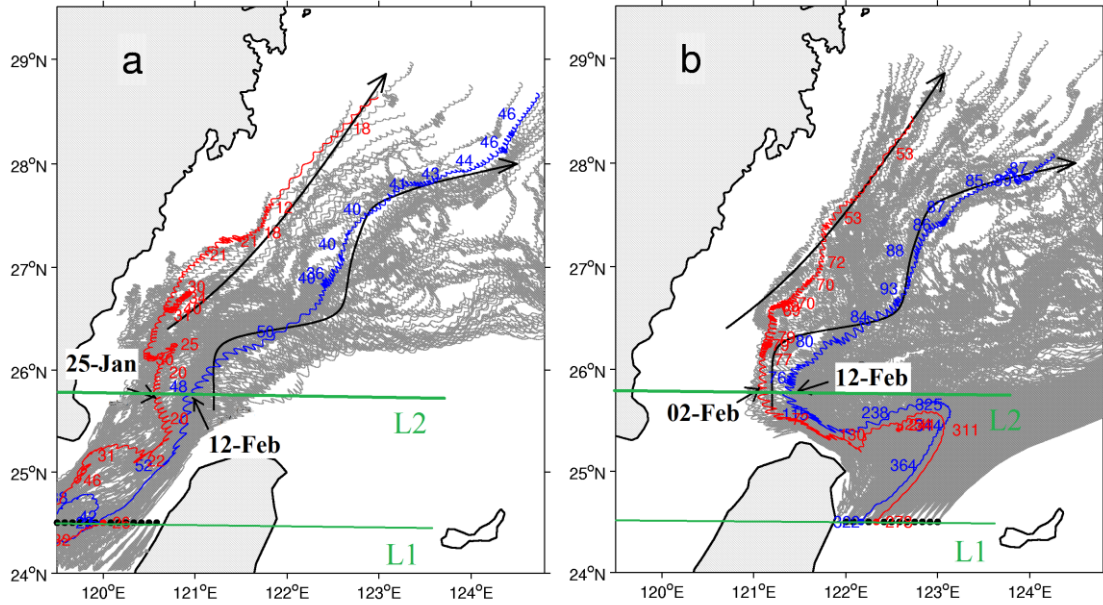
964

965

966

967

968

969

Figure 14: Mean currents (upper panels) and synoptic fluctuations (EOF1 in middle panels and EOF2 in bottom panels) in winters of 2010-2013. The black arrows in the upper panels show the velocity (m/s) in the layer of VMV with the color representing the current speed. The two blue arrows with label IB and OB represent the flow axes of the inshore branch and offshore branch, respectively. The black arrows in the middle panels and bottom panels represent the EOF components (m/s) with their magnitude represented by color scales.

Figure 15: Traces of TSC water (a) and Kuroshio water (b) in winter, with the variation of surface currents north of Taiwan (c). The green lines L1 and L2 indicate the starting latitude of the tracers (24.5 °N) and the latitude which is representative for synoptic fluctuations north of Taiwan (25.8 °N), respectively. The black dots represent the release locations of tracers originated from line L1. The gray lines show the entire trajectories of the tracers. The red lines and blue lines are selected trajectories, which are close to the inshore branch and offshore branch, 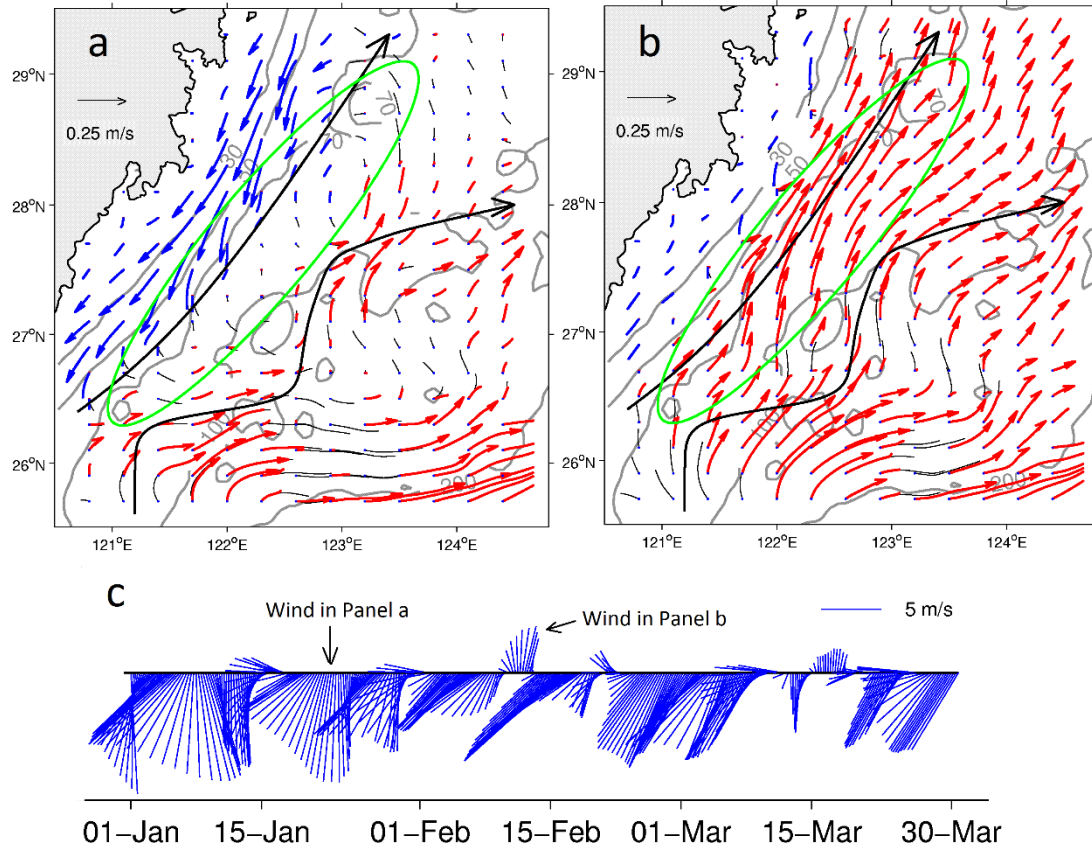respectively. The dates show the times when selected tracers cross the latitude indicated by line L2. The numbers are the depths of the tracers, which are labeled at an interval of six days. The two black arrows represent the two TWC branches.

Figure 16: The VMV under the northeasterly wind (a) and southwesterly wind (b). Panel (c) shows the variation of wind in winter. Blue vectors and red vectors show the southwestward coastal current and the northeastward TWC, respectively. Gray contours indicate the 30, 50, 70, and 100 m isobaths. The two black arrows represent the two TWC branches. The green ellipse indicates the inshore area with significant fluctuation.